IEEE Access
Multidisciplinary | Rapid Review | Open Access Journal

Received 1 September 2023, accepted 26 October 2023, date of publication 2 November 2023, date of current version 9 November 2023.

Digital Object Identifier 10.1109/ACCESS.2023.3329812

RESEARCH ARTICLE

Path Loss Based Wireless Capsule Endoscope Localization Using Machine Learning Regression

UMMA HANY[1], NAFE MUHTASIM HYE[1], AND LUTFA AKTER[2]
[1]Department of Electrical and Electronic Engineering, Ahsanullah University of Science and Technology, Dhaka 1208, Bangladesh
[2]Department of Electrical and Electronic Engineering, Bangladesh University of Engineering and Technology, Dhaka 1205, Bangladesh

Corresponding author: Umma Hany (uhany.eee@aust.edu)

This work was supported in part by the AUST Internal Research Grant (3rd Round) under the AUST Research Policy (ARP) of Ahsanullah University of Science and Technology (AUST), Dhaka, Bangladesh, and in part by the Basic Research Grant of Bangladesh University of Engineering and Technology (BUET), Dhaka, Bangladesh.

ABSTRACT Localization of wireless capsule endoscope (WCE) while it travels through the Gastrointestinal (GI) tract is required to find the exact location of the intestinal lesions. In this paper, we propose a method of localizing the WCE in the small intestine by applying machine learning-based regression algorithms on the ultra-wideband (UWB) and medical implant communication service (MICS) band signal. The path loss of the signals received by sensor receivers placed on the body surface is used as the input features to find the 3D x-y-z position of the WCE. To improve the accuracy of localization, we estimate the smoothed path loss by applying local linear regression moving average (LLRMA) and local weighted linear regression (LWLR) on the scattered path loss to minimize the path loss deviations caused by the dielectric properties of human body tissues. Then, we apply five machine learning regression algorithms namely Decision Tree (DT), Random Forest (RF), Extreme Gradient Boosting (XGB), Linear Regression (LR), and K-Nearest Neighbors (KNN) on both the scattered and smoothed path loss to localize 2443 mapped positions of the WCE in the small intestine trajectory model. We also analyze the impact of the number of sensor receivers and the network topology of the sensor array on the accuracy of localization. It is observed that the localization accuracy is significantly improved by applying all the regression algorithms on the smoothed path loss data. For the smoothed dataset, the best accuracy with 0.21 *mm* and 0.22 *mm* root mean square error (RMSE) is achieved by applying the KNN regression method on UWB and MICS path loss model, respectively using 48 sensor receivers. Additionally, it is also observed that with the UWB and MICS path loss, KNN shows 0.22 *mm* and 0.27 *mm* RMSE on the smoothed path loss using only 8 sensor receivers with a computational time of 0.004 *sec* and 0.005 *sec*, respectively.

INDEX TERMS WCE localization, computational and artificial intelligence, machine learning regression.

I. INTRODUCTION

The wireless capsule endoscope is used to diagnose the lesions in the GI tract. For proper diagnosis, the exact position of the lesions is required to be known which can be obtained by localizing the WCE in the GI tract while it travels through it. Several state-of-the-art works on WCE localization are reported in the literature [1], [2]. The WCE can be localized using the magnetic field strength, the radio signal strength indicator (RSSI), time of arrival (TOA), direction of arrival (DOA), time difference of arrival (TDOA), hybrid method, etc. [3], [4], [5], [6], [7], [8], [9], [10], [11], [12], [13], [14], [15], [16].

IEEE 802.15.6 standard RF frequency bands are recommended for wireless body area networks (WBAN) applications with a wide range of data rates with low energy consumption, lower range, and large number of nodes with security features [17]. Therefore, we focus on RF-based WCE localization using IEEE 802.15.6 standard frequency bands as it does not have any known adverse health effects and it ensures high data rate secure wireless communication using miniature nodes with extremely low power consumption.

The associate editor coordinating the review of this manuscript and approving it for publication was Daniel Augusto Ribeiro Chaves.

Federal Communications Commission (FCC) recommends the medical implant communication service (MICS) band for implant applications [17]. Short-range, high-data-rate wireless communication using UWB frequency bands is also defined in the IEEE standard 802.15.6 in the vicinity of, or inside, a human body [17] and is suitable and safe for implantable devices with less interference with other radio devices [18]. The UWB signal propagation models for implantable devices are presented in [17], [19], and [20].

The RSSI of the externally placed sensor receivers on the body surface can be used to localize the WCE while it travels through the GI tract using either triangulation, trilateration or weighted centroid localization (WCL) techniques [21], [22], [23], [24], [25], [26], [27], [28], [29], [30], [31], [32]. In [21] and [22], the authors use the signal strength measured by the wearable antenna array to find the 2*D* position of the in-vivo RF signal using triangulation and report an average error of 37.7 *mm*. The authors in [11] propose RSSI-based triangulation for WCE localization using 8-64 receiver sensors with a three-dimensional range of 268 × 323 × 312 *mm* and report root mean square error (RMSE) of 34 *mm* using 64 sensors. The authors in [23], [24], [25], [26], and [27] propose MICS path loss-based and the authors in [28] and [29] propose UWB path loss-based WCE localization using weighted centroid localization (WCL) with 3D sensor array of multiple receivers. In [23], the authors use 600 × 600 × 600 *mm* dimension sensor array for WCE localization and report 5.15 *mm* average error with known path loss parameters and prior knowledge of distance and real positions for the position calibration. In [24] and [25], the authors propose WCE localization with a 920 × 920 × 920 *mm* sensor array and report 6.27 *mm* and 7.28 *mm* average localization error, respectively. However, in [24] and [25], the distance is calculated using known path loss parameters and the degree of distance in [24] and the calibration coefficient in [25] are calculated either by using the maximum value of distance or by using linear least square regression of the estimated and real positions of the capsule. Thus, the methods in [23], [24], and [25] are not robust to path loss estimation errors and are dependent on prior knowledge of the distance and real positions. In [26] and [27], the authors use 920 × 920 × 920 *mm* sensor array and propose different MICS band path loss estimation methods to localize the WCE with 24.53 *mm* and 23.6 *mm* RMSE, respectively using the estimated path loss raised to a degree. However, the authors in [26] propose a heuristic method of degree estimation that is dependent on the maximum value of path loss and the maximum distance. The authors in [28] and [29] apply the MIMO diversity scheme and maximum likelihood (ML) estimation method to mitigate the effect of UWB path loss deviations and propose path loss-based position-bounded WCL for WCE localization using 920 × 920 × 920 *mm* sensor array and report 5.14 *mm*, and 6.2 *mm* RMSE, respectively. However, due to the size and space limitation, higher-order diversity antennas are difficult to be equipped in the capsule, and only 3-dB diversity gain is recommended in [33] for space diversity due to the high correlation between different on-body receiver locations. Moreover, the position bounds in [27], [28], and [29] and the calibration process in [28] are dependent on the small intestine's known dimension. Further in [28] and [29], the authors use the UWB propagation model developed for the human chest [19] which is not suitable for path loss modeling in the small intestine. In [31], the authors propose UWB RSS-based localization of WCE using a centroid algorithm and analyze the impact of the number of sensors and their locations on positioning accuracy. The authors in [31] report 34.12 *mm* RMSE using 20 sensors to estimate 64 positions of WCE in the small intestine where 48 positions are used to optimize the nonlinearity exponent of the localization algorithm and the remaining 16 positions are used to test the performance. In [32], the authors propose UWB smoothed path loss degree-based weighted centroid localization (SPLD-WCL) for WCE localization and also compute the cramer rao lower bound (CRLB) as the benchmark of accuracy to evaluate the performance. The authors in [32] report 6.83 *mm* RMSE using 48 sensor receivers using 200 × 200 × 200 *mm* dimension sensor array. However, the proposed methods in [23], [24], [25], [26], [27], [28], [29], [30], [31], and [32] require the reference positions of the sensor receivers to estimate the position of the WCE using WCL, and the accuracy of the proposed methods is greatly influenced by the reference positions of the sensor receivers. In [13], a hybrid method using camera motion tracking and RSSI-based WCE localization is proposed with an average localization error of 23 *mm*. In [16], the authors propose fusion-based hybrid localization using vision and IMU sensors and report 9.5 *mm* RMSE.

The above localization methods are influenced by the RF signal propagation due to the non-homogeneous tissue properties of the human body. In [34], the authors exploit spatial sparsity to estimate the position of the emitter in 200 × 200 *mm* range using the tissue-adaptive method without estimating the time of arrival (ToA) or path loss. The authors in [34] use convex optimization theory and l_1-norm minimization to estimate position and report less than 7.5 *mm RMSE* with perfectly known tissue structure and less than 8.8 *mm* with approximately known tissue structure with some levels of uncertainties. In [35] and [36], new approaches that are robust to channel estimation errors are proposed using RSSI-based maximum likelihood (ML) localization using finite impulse response (FIR) and particle filter to find the transition model of the capsule within 400 × 400 × 200 *mm* range and report 15 *mm RMSE* using FIR filter and 7 *mm RMSE* using particle filter-based approach. The authors in [37] propose UWB RSS-based WCE localization using compressive sensing and variable noise level (VNL) kalman filter and report 35-60 *mm* localization error based on the frequency of operation.

Recently, deep learning and machine learning algorithms are applied in genetics and other biomedical applications for the prediction, classification, and localization of different particles and objects [38], [39], [40], [41], [42], [43], [44].

Among those, few methods using artificial intelligence and neural network are reported on GI organ classification and WCE localization using the WCE images or videos [41], [42], [43], [44]. In [41] and [42], the authors apply different classification tools such as neural networks, brute force, and vector quantization algorithms to classify different regions of the GI tract by recognizing the MPEG-7 image descriptor features of the images received from the WCE and apply principle component analysis to reduce the dimension of the features. The authors in [41] report 86.12% average accuracy using neural network and the authors in [42] report 95.19% and 94.49% average accuracy using brute force and vector quantization, respectively. In [43], the authors propose the geometric visual odometry (VO) method for WCE localization in the GI lumen and extend the artificial neural network (ANN) to augment the geometric method to achieve higher accuracy and obtain mean absolute error of 0.79 ± 0.51 *cm*, for a distance of 19.6 *cm*. The authors in [44] propose a deep learning algorithm to classify GI organs and report average accuracy of 0.98, 0.96, 0.87, and 0.87 for the esophagus, stomach, small bowel, and colon, respectively.

In summary, though there have been several works on WCE localization, the accuracy of the methods is highly influenced by human body channel parameters, distance, and reference positions. Additionally, to the best of our knowledge, no research works are reported in the literature on WCE localization using artificial intelligence or neural networks on the RSSI or path loss data. Hence, a data-driven localization approach that is independent of human body channel, distance, and reference positions might be a good candidate for WCE. Therefore, there is a scope to apply machine learning or deep learning-based algorithms on the RSSI or path loss data and observe the accuracy of WCE localization.

In this paper, we propose a novel method of WCE localization by applying the path loss smoothing and machine learning regression algorithms on the smoothed path loss data. We develop the proposed WCE localization platform in MATLAB which includes a 3D small intestine trajectory model and a 3D sensor array of 4 to 48 sensor receivers that are used to measure the RSSI of the received signal and to obtain the path loss data. In this paper, we generate the scattered path loss data for 2443 traveling positions of the WCE in the small intestine trajectory model in 1 *mm* resolution considering six different sensor placement topologies and three different dimensions of the sensor array for different human body size. The distance between the mapped positions of the WCE in the small intestine and the reference positions of the sensor receivers are used to generate the UWB and MICS path loss using the path loss statistics extracted in [20] and [45] using the in-body to on-body in-vivo measurements scenario and the deep tissue implant to body surface scenario, respectively. However, due to the body tissue properties, the path loss is highly deviated which is required to be minimized to improve the localization accuracy. We apply two path loss smoothing methods namely local linear regression moving average (LLRMA) and local weighted linear regression (LWLR) to minimize the path loss deviation by finding the best-fitted path loss. Finally, five machine learning regression methods namely Decision Tree (DT), Random Forest (RF), Extreme Gradient Boosting (XGB), Linear Regression (LR), and K-Nearest Neighbors (KNN) are applied on the scattered as well as on the smoothed path loss to predict the position of the WCE in the small intestine. Five-fold cross-validation is applied using all eight scenarios to verify the accuracy of localization at 2443 target points of the capsule. As we can see that for all the sensor placement topologies and dimensions of the sensor array, a significantly high accuracy of localization is obtained by applying ML regression method on the smoothed path loss. Using a minimum of 8 sensor receivers, we obtain 0.22 *mm* and 0.27 *mm* RMSE using KNN on the LWLR smoothed path loss in only 0.004 sec and 0.005 sec computational time using UWB and MICS band path loss, respectively. Whereas using 48 sensor receivers, KNN obtains 0.21 *mm* and 0.22 *mm* RMSE with UWB and MICS path loss, respectively. Thus, it is observed that our proposed WCE localization method using ML regression on the smoothed path loss can obtain significantly high accuracy without any prior knowledge of channel parameters, distances, reference positions, sensor placement topology, and dimensions of the human body.

II. SYSTEM MODEL

We propose a path loss-based WCE localization system using path loss smoothing methods and machine learning regression. The proposed system model is shown in Figure 1. In our proposed system, the WCE travels through the small intestine model and a set of sensor receivers are used to receive the RF signal propagated from the WCE. The small intestine is modeled and mapped with 2443 traveling positions of the capsule. The sensor receivers are placed on the body surface or a wearable sensor array around the waist to measure the received signal strength indicator (RSSI) of the received signals. The path loss is computed using the measured RSSI of the sensor receivers. The path loss is modeled considering the body tissue properties for in-body to on-body in-vivo measurement scenarios. Due to the body tissue properties, the generated path loss is randomly scattered around a mean. To localize the WCE accurately, we apply two path loss smoothing methods to minimize the path loss deviations. The smoothed path loss is then split into training and test datasets and applied to the machine-learning regression models for WCE localization.

In our proposed WCE localization system, the path loss between the capsule transmitter and sensor receivers is used to localize the position of the WCE in the small intestine. Thus, in our system, path loss data is used as the input variable and the $3D$ position of the WCE in the small intestine is used as the output variable. Practically, we obtain the path loss data by measuring the RSSI of the 48 sensor receivers and the transmitted power of the WCE as shown below

$$L_i(dB) = P_T(dBm) - RSSI(dBm), \tag{1}$$

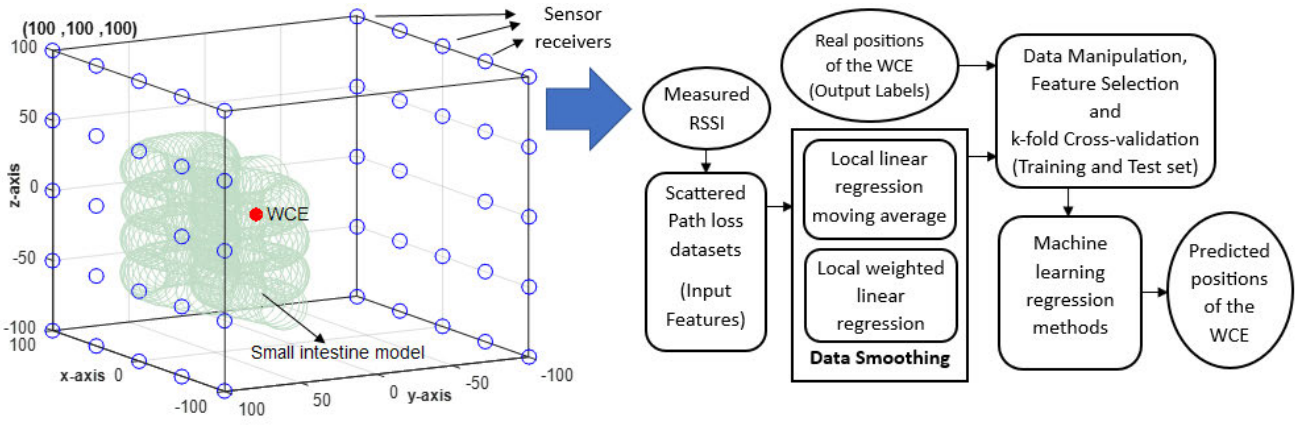

FIGURE 1. System block diagram.

where L_i is the path loss between the WCE and the i^{th} sensor receiver and P_T is the transmitted power of the capsule. We generate the input and output datasets for simulation using the following path loss model and the small intestine model.

A. PATH LOSS MODEL

Path loss attenuates with the distance between the transmitter and receivers. The signal propagation path loss between the capsule transmitter and the body-surrounded sensor receivers is scattered due to the material dielectric properties of different human body layers. We use both UWB and MICS band path loss models to generate the path loss between the capsule transmitter and sensor receivers.

1) UWB PATH LOSS MODEL

The UWB scattered path loss can be represented using the following linear path loss model,

$$L_i = \alpha \left(\frac{r_i}{r_0}\right) + L(r_0) + X(0, \sigma_L^2), \tag{2}$$

where, α, r_i, r_0, and $L(r_0)$ denotes the fitting constant, the separation distance between the capsule transmitter (Tx) and the i^{th} sensor receiver (Rx), reference Tx-Rx distance and the path loss in dB at reference distance r_0, respectively. The statistical distribution $X(0, \sigma_L^2)$ of the shadowing term follows a Gaussian distribution model with zero mean and standard deviation of σ_L. The best-fitted mean path loss excluding the scattering term $X(0, \sigma_L^2)$ can be expressed as

$$\overline{L}(r_i) = \alpha \left(\frac{r_i}{r_0}\right) + L(r_0). \tag{3}$$

2) MICS PATH LOSS MODEL

We use the following logarithmic path loss model to represent the MICS band scattered path loss,

$$L_i = 10\gamma \log_{10}\left(\frac{r_i}{r_0}\right) + L(r_0) + X(0, \sigma_L^2), \tag{4}$$

where, γ, r_i, r_0, $L(r_0)$ and $X(0, \sigma_L^2)$ denote the logarithmic path loss exponent, the Tx-Rx separation distance, the reference distance, the reference path loss in dB, and the scattering term with zero mean and σ_L path loss deviations, respectively. The best-fitted mean path loss can be expressed as

$$\overline{L}(r_i) = 10\gamma \log_{10}\left(\frac{r_i}{r_0}\right) + L(r_0). \tag{5}$$

The standard deviation, σ_L of both the UWB and MICS path loss can be given as

$$\sigma_L = \sqrt{\frac{1}{N}\sum_{i=1}^{N}(L_i - \overline{L}(r_i))^2}, \tag{6}$$

where N is the total number of sensor receivers.

B. SMALL INTESTINE TRAJECTORY MODEL

We develop a spiral-shaped $3D$ small intestine model to map the x-y-z coordinate positions of the capsule transmitter using the following three equations

$$x_r = acos(t), \tag{7}$$
$$y_r = b - dsin(2t), \tag{8}$$
$$z_r = ht, \tag{9}$$

where t is from -15 to 3π with 0.01 increment. Depending on the value of a, b, d, and h, the dimension of the small intestine model can be changed.

C. 3D SENSOR ARRAY

We consider a body-surrounded 3D sensor array including 8 to 48 sensor receivers to receive the RF signal transmitted from the capsule transmitter. We apply six (06) different topologies of sensor placement as shown in Figure 2. We also consider three different dimensions of the sensor array and two different dimensions of the small intestine for normal, overweight, and obese human body size as illustrated in Figure 3 and summarized in Table 1.

TABLE 1. Dimension of the sensor array and small intestine.

	Normal Fig. 3(a)	Overweight Fig. 3(b)	Obese Fig. 3(c)
Sensor array	$200 \times 200 \times 200\ mm$	$400 \times 400 \times 200\ mm$	$600 \times 600 \times 200\ mm$
Small intestine	$120 \times 70 \times 120\ mm$	$200 \times 100 \times 170\ mm$	$200 \times 100 \times 170\ mm$

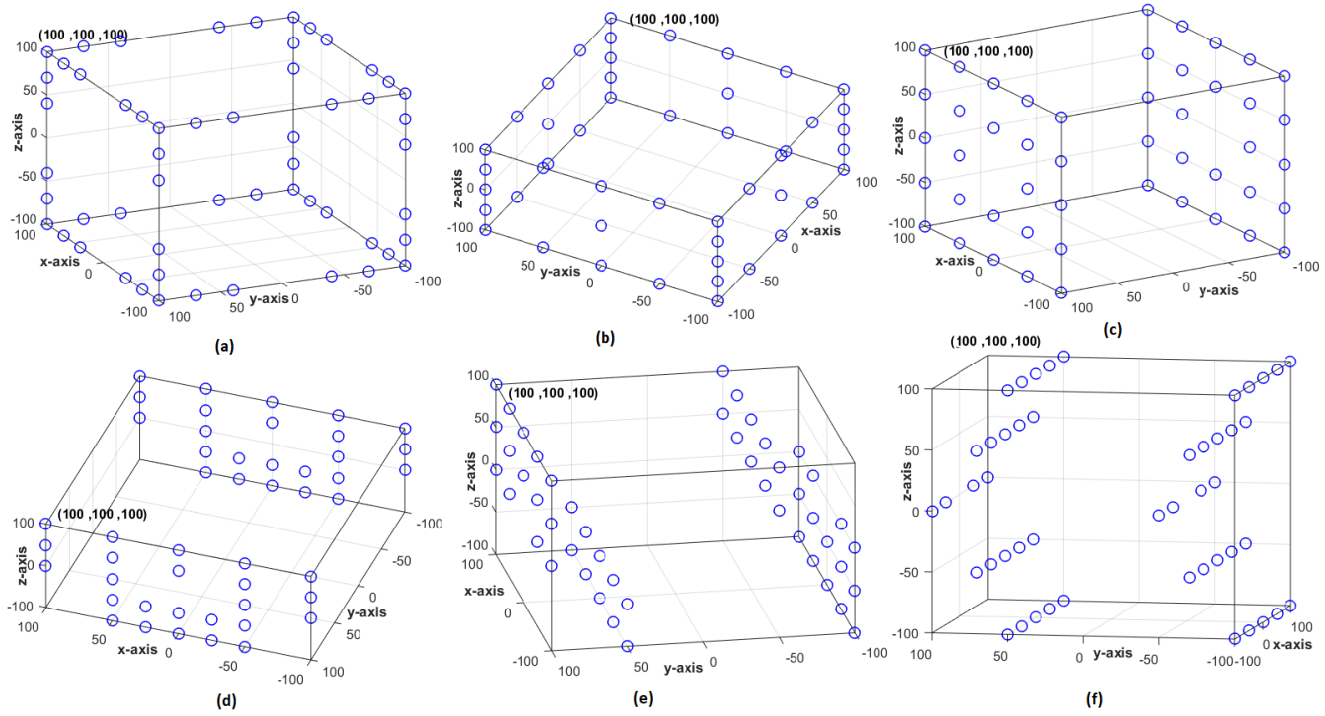

FIGURE 2. Sensor placement topologies.

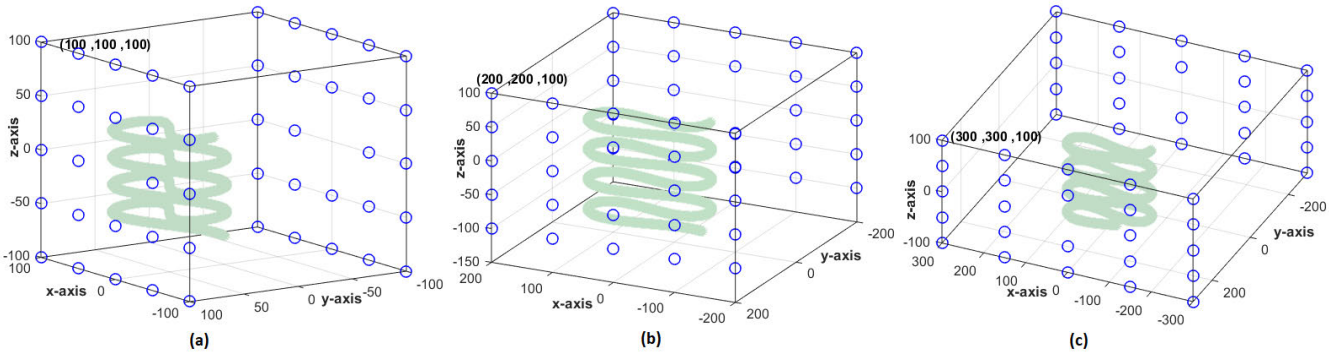

FIGURE 3. Dimension of the sensor array and the small intestine; (a) Normal body size: Sensor array (200 × 200 × 200 *mm*) and small intestine (120 × 70 × 120 *mm*), (b) Overweight body size: Sensor array (400 × 400 × 200 *mm*) and small intestine (200 × 100 × 170 *mm*), (c) Obese body size: Sensor array (600 × 600 × 200 *mm*) and small intestine (200 × 100 × 170 *mm*).

III. DATA GENERATION

As the path loss attenuates with the distance between the transmitter and sensor receivers, we consider path loss as a measure of distance. We generate the path loss as the input datasets and the real positions of the capsule transmitter as the output datasets of the WCE localization system. The input and output data generation process is explained below.

A. PATH LOSS DATA GENERATION

We generate both the UWB and MICS band path loss datasets as the input of the system. Short-range, wireless communication using UWB frequency inside a human body is specified in the IEEE standard 802.15.6 and characterized by very low power consumption, the smaller size of the antennas, and a higher data rate [17], [20]. In [20], the

TABLE 2. UWB and MICS path loss model for ingestible devices [20], [45].

Band	Scenario	$L(r_0)$	α	σ_L
UWB	In-body to on-body in-vivo measurements	41.5635 dB	4.337	4.6007
MICS	Deep tissue implant to body surface	47.14dB	4.26	7.85

statistics of the linear path loss model as shown in eq. (2) are extracted for the UWB frequency band covering from 3.1 to 6 GHz using in-vivo measurements. During the in-vivo measurements, the on-body receiving antennas are placed on the abdomen and the in-body positions are located to be surrounded by either colon or small bowel indistinctly. The extracted statistics of the UWB path loss are specified in Table 2.

MICS band is recommended for in-body communication for implant applications [17]. In [45], the authors use a 3D visualization platform to extract the path loss statistics of the MICS band logarithmic path loss model as shown in eq. (4). The 3D platform in [45] includes a three-dimensional human body model, a three-dimensional full-wave electromagnetic field simulator (i.e. HFSS 1), and an implantable (or body surface antenna). The 3D human body model includes frequency-dependent dielectric properties of 300+ parts in a male human body with 2 *mm* resolution. The statistics of the MICS band path loss using deep tissue scenario are specified in Table 2. The deep tissue implant scenario considers endoscopy capsule applications for the upper stomach and lower stomach.

We generate the UWB and MICS band scattered path loss for varying positions of the WCE in the small intestine using eqs. (2) and (4) using the path loss statistics as specified in Table 2. The Tx-Rx separation distance r_{ij} for 2443 varying positions of the WCE is calculated as shown below

$$r_i = \sqrt{(x_r - x_i)^2 + (y_r - y_i)^2 + (z_r - z_i)^2}, \tag{10}$$

where, (x_r, y_r, z_r) are the coordinates of the real position of the capsule transmitter and (x_i, y_i, z_i) are the coordinates of the reference position of the i^{th} sensor receiver.

We generate the UWB and MICS band path loss for 2443 varying positions of the WCE in the small intestine considering six topologies of sensor deployment as shown in Figure 2 and the three dimensions of the sensor array and small intestine as presented in Table 1 and Figure 3.

B. POSITION DATA GENERATION

We generate 2443 mapped 3D positions of the WCE in the small intestine trajectory model using eqs. (7), (8) and (9) considering two different dimensions of the small intestine for different body sizes. The parameters used to generate the x-y-z coordinate positions for the two dimensions of the small intestine are given in Table 3. To generalize the proposed methods with large and more varied datasets, the mapped positions are localized using 8 different sensor placement

TABLE 3. Small intestine trajectory model parameters.

Dimension of the small intestine	a	b	d	h
$120 \times 70 \times 120\ mm$	60	50	20	4
$200 \times 100 \times 170\ mm$	100	80	20	7

topologies by varying the dimensions and positions of the sensor receivers as shown in Figures 2 and 3. By varying the dimensions and positions of the sensor receivers, the Tx-Rx separation distance as shown in eq. 10 and the scattered path loss as shown in eqs 2 and 4 are also varied. Thus, 8 different datasets are generated for 8 different scenarios as summarized in Table 4.

IV. DATA SMOOTHING

We apply the following two data smoothing methods to minimize the deviations of path loss.

A. LOCAL LINEAR REGRESSION MOVING AVERAGE

Path loss is estimated as a measure of Tx-Rx distance and to compute the weight of the reference positions of the sensor receivers. The propagation path loss is scattered due to the shadowing effect caused by the non-homogeneous human tissue dielectric properties. To get an accurate estimate of the path loss, the scattering of the path loss is required to be minimized. The capsule travels M possible points through the small intestine. The best-fitted path loss of the adjacent traveling location points can be estimated as

$$\overline{L}_{ik} = c_1 k + c_2, \tag{11}$$

where, $k = (j - n_L) : (j + n_R)$ is the range of $n_R + n_L + 1$ adjacent location points of the capsule at j^{th} instant assuming $n_R = n_L$, n_L is the lower bound and n_R is the upper bound of the adjacent location points, c_1 and c_2 are the path loss exponents. The matrix of the measured path loss of adjacent location points and the set of the $n_R + n_L + 1$ adjacent location points are expressed as

$$L = \begin{pmatrix} L_{i(j-n_L)} \\ L_{i(j-n_L+1)} \\ \vdots \\ L_{i(j+n_{R-1})} \\ L_{i(j+n_R)} \end{pmatrix} \quad and \quad K = \begin{pmatrix} j - n_L \\ j - n_{L+1} \\ \vdots \\ j + n_{R-1} \\ j + n_R \end{pmatrix} \tag{12}$$

The path loss exponents are estimated by using linear least square regression of the scattered path loss measured at the adjacent location points of the capsule as follows

$$C = (K^T K)^{-1} K^T L, \tag{13}$$

where, $\mathbf{C}$ is the matrix containing the path loss exponents c_1 and c_2 as follows

$$C = \begin{pmatrix} c_1 \\ c_2 \end{pmatrix} \tag{14}$$

Using the extracted path loss exponents c_1 and c_2, we can estimate the smoothed path loss, PL_{ij} between the i^{th} sensor

TABLE 4. Different variables containing the generated and smoothed datasets.

Name	Variable	Content	Dimension	No. of Scenarios
Position of the sensor receivers (Rx)	$S(x_i, y_i, z_i)$	Column 1 to 3 containing 48 x-y-z coordinate positions of the 48 sensor receivers	48×3	8
Real positions of the WCE transmitter (Output labels)	$P(x_r, y_r, z_r)$	Column 1 to 3 containing 2443 real x-y-z coordinate positions of the WCE	2443×3	8
Tx-Rx separation distance	r_i	Each of the Columns 1 to 48 includes 2443 Tx-Rx separation distances measured between the 48 sensor receivers to the 2443 traveling positions of the WCE.	2443×48	8
Scattered Path loss (Input features)	L_i	Each of the Columns 1 to 48 includes 2443 scattered path loss data measured by 48 sensor receivers for 2443 traveling positions of the WCE.	2443×48	8
Smoothed Path loss (Input features)	PL_{ij}	Each of the Columns 1 to 48 includes 2443 smoothed path loss data measured by 48 sensor receivers for 2443 traveling positions of the WCE.	2443×48	8

receiver and j^{th} location point by averaging the best fitted mean path loss of the adjacent location points as

$$PL_{ij} = \frac{1}{(n_R + n_L + 1)} \sum_{k=j-n_L}^{j+n_R} \overline{L}_{ik} = \frac{1}{(n_R + n_L + 1)} \sum_{k=j-n_L}^{j+n_R} (c_1 k + c_2). \quad (15)$$

We also apply the following kernel adaptation method to set the lower bound and upper bound of the span.

$$\begin{aligned} \text{If } j < n_{th} \text{ then } & n_R = j - 1; \\ & n_L = n_{th}; \\ \text{else if } j > M - n_{th} \text{ then } & n_L = M - j; \\ & n_R = n_{th}; \\ \text{else } & n_R = n_L = n_{th}; \end{aligned} \quad (16)$$

where, n_{th} is set as the lower bound and upper bound of the span for most of the location points. However, for few of location points near the start and destination of the capsule, the lower bound and upper bound of the span is updated as shown in eq. (16).

B. LOCAL WEIGHTED LINEAR REGRESSION

Local weighted linear least square regression is a non-parametric regression that finds the best-fitted smooth curve for fitting to the local neighboring data points in a span using weighted least squares. It defines a regression weight function for the data points contained within the span and assigns less weight to points further away or the outliers [46], [47]. The best-fitted path loss for the k local traveling points can be expressed using the following linear equation,

$$\overline{L}_{im} = \gamma B_m, \quad m = 1, 2 \ldots k \quad (17)$$

where, B_m is the m^{th} local point in a span and γ is the fitting constant. The local weighted linear regression finds γ to minimize the following

$$\sum_{m=1}^{k} w_m (L_{im} - \gamma B_m)^2,$$

where, w_m are the weight of the k local points. More weights are assigned to points near the target and less weight is assigned to points further away. The weight is defined by the tricube function as follows

$$w_m = \left(1 - \left|\frac{(B_j - B_m)}{d(B)}\right|^3\right)^3, \quad (18)$$

where B_j is the particular data point at which we are evaluating the regression and $d(B)$ is the distance of the data point B_j to the most distant data point within the span. The weight is defined in such a way that the data point to be smoothed has the largest weight and the data points outside the span have zero weight. If the vector of the path loss of the neighboring points is $\mathbf{L}$, the vector of the k local points within a span is $\mathbf{B}$ and their corresponding weight vector is $\mathbf{W}$, then γ can be determined using locally weighted linear least square as follows

$$\gamma = (B^T W B)^{-1} B^T W L. \quad (19)$$

Now the smoothed path loss of 2443 traveling location points can be computed using the best-fitted path loss of the specific location point as follows

$$PL_{ij} = \overline{L}_{ij} = \gamma B_j. \quad (20)$$

Table 4 summarizes the contents, dimensions, and quantity of the generated and smoothed datasets for the 8 scenarios.

V. WCE LOCALIZATION USING ML REGRESSION

We apply five machine-learning regression algorithms for WCE localization. The methodologies are explained below.

A. DATA MANIPULATION AND FEATURE SELECTION

The following data manipulation and feature selection methods are applied.

1) DATA LABELING AND CONCATENATION

In our WCE localization system, there are 48 sensor receivers to receive the RF signal transmitted by the capsule transmitter from 2443 varying positions of WCE in the small intestine. To compare the accuracy of different scenarios based on the body size and sensor placement topology, we generate the received signal path loss for 8 different scenarios.

In our proposed regression models, the scattered path loss of the received signals by the 48 sensor receivers are used as the input features and the 3-dimensional x-y-z coordinate positions of the WCE are used as the output labels. To compare the accuracy, we also use the smoothed path loss of the 48 sensor receivers as the input features and the x-y-z positions as the output labels.

Finally, the path loss data of 48 sensor receivers (input features) and the corresponding x-y-z coordinate positions (output labels) are concatenated in a single data file. The concatenated data files include all the path loss data of 48 sensor receivers and their corresponding 3D x-y-z coordinate positions.

2) FEATURE SELECTION

Feature selection discards less important features of the data. We apply feature selection to select the most important features of the data. We consider the input features measured by the 8 sensor receivers at the corner points of the sensor array first and then increase the number of input features from 8 to 48 sensor receivers with an increment of 8 to analyze the performance. We also consider the 4 input features of the front-side sensor receivers to analyze the performance. In this way, we analyze the impact of the number of sensor receivers and the input features on the accuracy of localization. We also could identify the important features and the minimum number of input features required to achieve the expected level of localization accuracy.

B. K-FOLD CROSS VALIDATION

The k-fold cross-validation is applied to split the datasets and to validate the test accuracy of all the datasets [48].

The datasets are split into training and test datasets. In the training phase, the input features of 8 to 48 sensor receivers or the path loss data are trained with the output labels or the 3D x-y-z position of the WCE. In the test phase, input features or path loss data are used to predict the x-y-z positions. The real x-y-z positions or output labels of the test data are used to verify the accuracy of localization. Both the scattered and smoothed path loss datasets are trained and tested using the k-fold cross-validation method.

We apply 5-fold cross-validation as follows:

1) The datasets are shuffled to 42 random states.

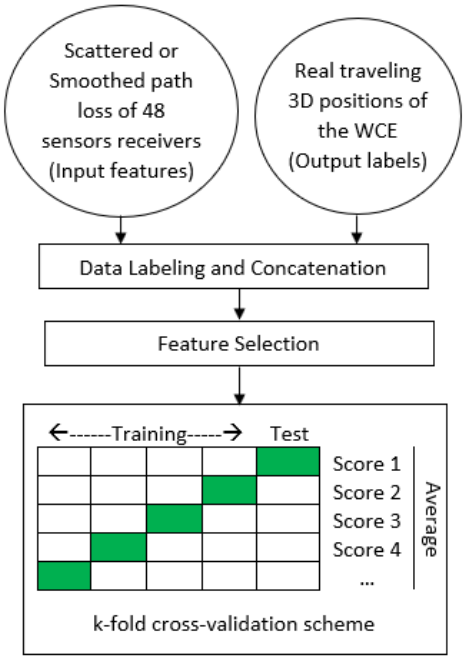

FIGURE 4. Data manipulation, feature selection, and k-fold cross validation.

2) We split the datasets into 5 groups each containing 20% of the total datasets.
3) For each of the groups:
   a) One of the group is taken as the test data set.
   b) The remaining groups are taken as a training data set.
   c) 5 Machine learning models are fitted on the training datasets and test datasets are evaluated.
   d) The evaluation score is recorded.
4) We evaluate the performance of the model by averaging the score of each sample group.

The system flow diagram of the data manipulation, feature selection, and k-fold cross-validation is shown in Figure 4.

C. MACHINE LEARNING REGRESSION METHODS

We apply several machine learning (ML) regression models for WCE localization to analyze the accuracy and computational effectiveness of the algorithms. Our proposed localization system model has a scope of having more than one input feature to localize the WCE in consecutive positions in the small intestine. Therefore, we employ five ML regression models namely Decision Tree (DT), Random Forest (RF), Extreme Gradient Boosting (XGB), Linear Regression (LR), and K-Nearest Neighbors (KNN) that are used to predict a continuous outcome based on the value of one or more input variables [49], [50], [51]. Regression analysis falls under supervised learning where the algorithm is trained with both input variables or features and output variables or labels [49]. In the training phase, we train the path loss input features to the corresponding labels of x-y-z

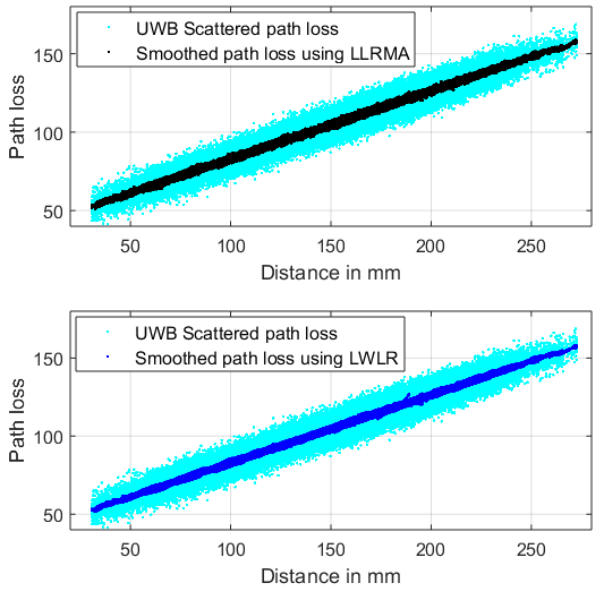

FIGURE 5. UWB scattered and smoothed path loss as a function of distance.

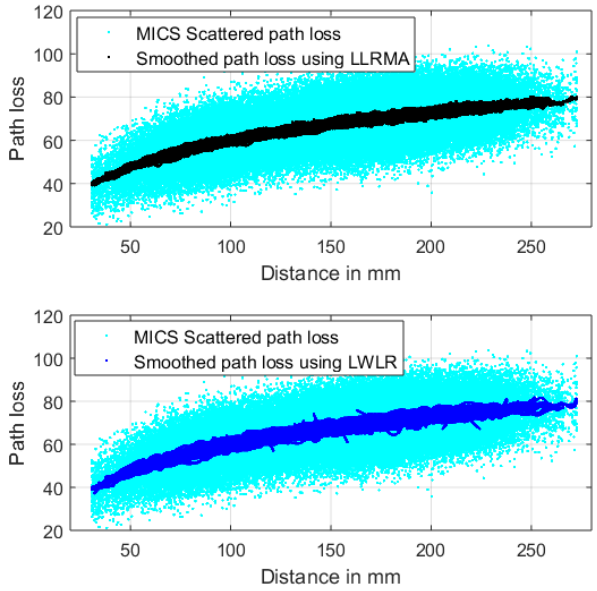

FIGURE 6. MICS scattered and smoothed path loss as a function of distance.

positions. In the test phase, the path loss data are applied to the ML regression models to predict the 3D position of the WCE. We apply both scattered and smoothed path loss using UWB and MICS bands to evaluate the performance of the applied ML regression models. We also evaluate the performance of the regression models by varying the input features or the number of sensor receivers.

VI. PERFORMANCE METRICS

We apply the Coefficient of Determination, R^2 to measure the accuracy of path loss estimation using the two smoothing methods. Usually, errors are used as the performance metric for regression problems. We use three performance metrics to evaluate the performance of the applied ML-based regression methods for WCE localization. The performance metrics are discussed below.

A. COEFFICIENT OF DETERMINATION, R^2

The coefficient of determination R^2 measures how well a statistical model predicts an outcome. The outcome is represented by the model's dependent variable. The lowest possible value of R^2 is 0, and the highest possible value is 1. The better a model is at making predictions, the closer the R^2 will be to 1. The formula for the coefficient of determination is as follows:

$$R^2 = 1 - \frac{RSS}{TSS}, \tag{21}$$

where RSS is the sum of squared residuals and TSS is the total sum of squares. We use R^2 to verify the performance of the proposed path loss estimation or smoothing methods. For the path loss estimation method, we calculate the coefficient of determination of path loss, R^2 as follows:

$$\begin{aligned} R^2 &= 1 - \frac{\sum(\text{Scattered path loss - Smoothed path loss})^2}{\sum(\text{Scattered path loss - Mean of scattered path loss})^2} \\ &= 1 - \frac{\sum(L_{ij} - PL_{ij})^2}{\sum(L_{ij} - \hat{L}_{ij})^2}. \end{aligned} \tag{22}$$

B. ROOT MEAN SQUARED ERROR (RMSE)

Root Mean Squared Error (RMSE) is the square root of the mean or average of the squared differences between predicted and expected target values in a dataset. It is calculated as follows.

$$\text{RMSE} = \sqrt{\frac{1}{M}\sum_{j}^{M}(P_j - \hat{P}_j)^2}. \tag{23}$$

where P_j is the j^{th} is the expected real x-y-z coordinate positions of the WCE in the dataset, $\hat{P}_j$ is the j^{th} predicted positions. The difference between these two values is squared, which results in a positive error value. The squaring also magnifies the larger errors.

VII. SIMULATION AND RESULTS

The proposed WCE localization system is developed in MATLAB and Python using a variety of popular data analysis tools and libraries. The libraries of Python include pandas, scipy.io, numpy, matplotlib. The regression models are developed using Scikit-Learn tools. The computational environment of simulation, training, and testing is based on a 64-bit Windows operating system with an x64-based Intel(R) Core(TM) i7-12700 CPU with 2.10 GHz processor and 32.00 GB of installed RAM. In addition, we leverage the NVIDIA GeForce RTX 3070 GPU for efficient computation.

The path loss data and position data are generated and smoothed in MATLAB. We generate the path loss datasets

TABLE 5. R^2 score of the path loss smoothing methods.

	UWB path loss model		MICS path loss model	
	LLRMA	LWLR	LLRMA	LWLR
R^2 score	0.9548	0.9547	0.4399	0.4547

using UWB and MICS path loss models as shown in eqs. (2) and (4) using the path loss parameters as specified in Table 2. The x-y-z coordinate positions in the small intestine are mapped using eqs. (7), (8) and (9) using the parameters as specified in Table 3. The path loss data and position data generation process is explained in Section III and the generated data variable are summarized in Table 4.

The path loss is randomly scattered due to the non-homogeneous human body tissue properties. Therefore, we apply two path loss smoothing methods: local linear regression moving average (LLRMA) and local weighted linear regression (LWLR). Figures 5 and 6 demonstrate the scattered path loss and the smoothed path loss using as a function of distance using UWB and MICS path loss models, respectively. As we can see in Figures 5 and 6 that the raw path loss is highly scattered around a mean and the two path loss smoothing methods minimizes the deviations significantly. We compute the R^2 score for the UWB and MICS path loss smoothing methods using eq. (22) for sensor topology (c) as shown in Figure 2(c). The R^2-scores of the smoothing methods are included in Table 5. It is observed from Table 5 that both smoothing methods perform reasonably well for both UWB and MICS channel models.

The data manipulation, feature selection, and cross-validation are applied in Python. The input path loss features of the 48 sensor receivers and the output labels are concatenated and cross-validated to split the data into 5 groups of 20% data and keep one of the groups as the test dataset and the remaining groups as the training datasets as shown in Figure 4. Then, we apply 5 different ML-based regression algorithms DT, RF, XGB, LR, and KNN on the training datasets and evaluated them with the test datasets. Each test set's performance score is then averaged to find the overall score.

A. PARAMETER SETTINGS

Each model is configured with specific parameters that contribute a crucial role in their performance. The Decision tree (DT) regression model is constructed using the *squared_error* criterion, which minimizes the sum of squared errors during the tree construction process. The maximum depth of the decision tree is configured as *None* or not restricted allowing the tree to grow until all the nodes are pure or until a specified stopping criterion is met. Additionally, the *best* split strategy is utilized to determine the optimal splitting point at each node.

The Random forest (RF) regressor is built with 100 decision trees (*n_estimators* : 100) and employed the squared error criterion for node splitting (*criterion* : *squared_error*). The maximum number of features considered at each split is set to 1.0, indicating that all features were eligible for selection (*max_features* : 1.0). The bootstrap sampling technique was applied to create each tree (*bootstrap* : *True*), and no restrictions were imposed on the maximum depth of the trees (*max_depth* : *None*).

The XGBoost (XGB) regressor utilizes the objective function of '*reg* : *squarederror*' to optimize the squared error loss during training. It employed 100 gradient-boosted trees (*n_estimators* : 100) and had no specified random seed for reproducibility (*random_state* : *None*). Other parameters were left with their default values.

In the case of Linear regression (LR), no specific parameter values were provided. The default settings were employed, including the option for fitting the intercept term (*fit_intercept* : *True*) and allowing the model to utilize multiple CPU cores if available (*n_jobs* : *None*).

Lastly, for the K-Nearest Neighbors (KNN) regression model, the number of neighbors considered is 5 (*n_neighbors* : 5), and the distance metric used for measuring similarity between data points is the Euclidean distance (*metric* : *minkowski*). The weights assigned to the neighbors were uniform (*weights* : *uniform*), meaning that all neighboring points have equal influence on the prediction.

B. PERFORMANCE USING REGULAR PATTERN

We consider six (06) different sensor placement topologies as shown in Figure 2 (a)-(f) considering the different strategies of sensor deployment. First, we consider that the sensor receivers are placed on plain surfaces of a regular pattern sensor array fixed on a wearable jacket or belt as shown in topologies (a) to (d) in Fig. 2. In sensor topology (a), the sensor receivers are placed as a cluster at the corner points of the cubic sensor array whereas in topology (b), the sensor receivers are placed on all the surfaces and edges of the cubic sensor array. Table 6 presents the obtained RMSE scores and computational time by applying the ML regression on the UWB scattered and smoothed path loss features using topologies (a) and (b). As we can see from the results in Table 6 that the RMSE drops significantly by applying the smoothing method LLRMA, whereas the computational time taken by the scattered and smoothed path loss is almost the same. However, as it is not easy to place the sensor receivers on the right and left surfaces of the sensor array, we propose topologies (c) and (d) where the sensor receivers are placed only on the front and back surfaces (x-z plane) and edges of the cubic array. The RMSE scores and computational time for both UWB and MICS path loss using topologies (c) and (d) are summarized in Table 7. To choose the best topology among the 04 sensor topologies (a) to (d) of regular patterns, the evaluation scores as presented in Table 6 and 7 are compared. For better visualization, Figure 7 compares the RMSE of the four topologies using the five ML regression methods on LLRMA smoothed path loss. It is observed that the RMSE scores and the computational time using the four regular sensor topologies are very close

TABLE 6. Evaluation scores using regular pattern sensor topologies (a) and (b) with normal human body dimensions.

	Topology (a)				Topology (b)			
UWB models	Scattered		LLRMA		Scattered		LLRMA	
ML regression	RMSE (mm)	Time (s)	RMSE (mm)	Time (s)	RMSE (mm)	Time (s)	RMSE (mm)	Time (s)
DT	9.46	0.066	1.31	0.064	9.23	0.074	1.23	0.066
RF	4.03	3.76	0.399	3.32	4.3	3.74	0.39	3.59
XGB	4.46	1.93	0.91	1.8	4.59	1.92	0.79	2.78
LR	2.79	0.011	0.58	0.011	2.81	0.012	0.56	0.012
KNN	2.34	0.023	0.25	0.021	2.26	0.021	0.26	0.024

TABLE 7. Evaluation scores using regular pattern sensor topologies (c) and (d) with normal human body dimensions.

	Topology (c)						Topology (d)					
UWB models	Scattered		LLRMA		LWLR		Scattered		LLRMA		LWLR	
ML regression	RMSE (mm)	Time (s)	RMSE (mm)	Time (s)	RMSE (mm)	Time (s)	RMSE (mm)	Time (s)	RMSE (mm)	Time (s)	RMSE (mm)	Time (s)
DT	9.73	0.045	1.28	0.042	1.05	0.038	9.69	0.046	1.19	0.04	0.89	0.035
RF	4.29	2.69	0.52	3.07	0.24	2.84	4.43	3.38	0.33	2.86	0.27	2.65
XGB	4.56	4.33	0.90	4.45	0.63	3.94	4.67	1.96	0.85	1.81	0.61	1.79
LR	3.004	0.0067	0.65	0.006	0.48	0.008	3.22	0.008	0.69	0.006	0.53	0.006
KNN	2.38	0.07	0.23	0.06	0.21	0.035	2.37	0.034	0.24	0.032	0.21	0.033
MICS models	Scattered		LLRMA		LWLR		Scattered		LLRMA		LWLR	
DT	27.21	0.04	1.90	0.044	1.64	0.043	26.85	0.047	1.83	0.043	1.79	0.042
RF	16.85	3.89	0.63	3.28	0.65	3.11	16.72	3.56	0.70	3.18	0.55	3.15
XGB	16.07	4.003	1.20	4.52	1.08	4.35	15.887	2.12	1.18	1.96	0.95	2.24
LR	13.42	0.007	1.72	0.008	2.75	0.008	13.62	0.007	1.58	0.007	2.84	0.01
KNN	15.25	0.07	0.25	0.068	0.22	0.036	15.40	0.035	0.25	0.031	0.21	0.036

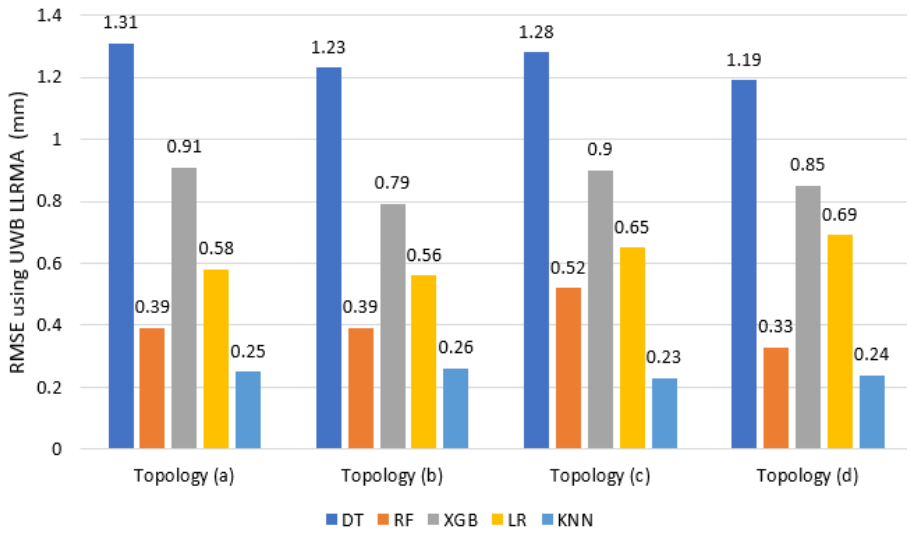

FIGURE 7. RMSE comparison of the four sensor topologies (a)-(d) using regular pattern.

to each other and KNN performs the best among the five regression methods with low computational time. Therefore, considering the real body shape, as it is easy to deploy the sensor receivers on the front and back surfaces of the sensor array, it may be concluded that topologies (c) and (d) are suitable regular pattern sensor topologies for the human body.

Table 7 also presents the RMSE scores by applying LWLR smoothing method on both UWB and MICS path loss considering normal body dimensions. To visualize the

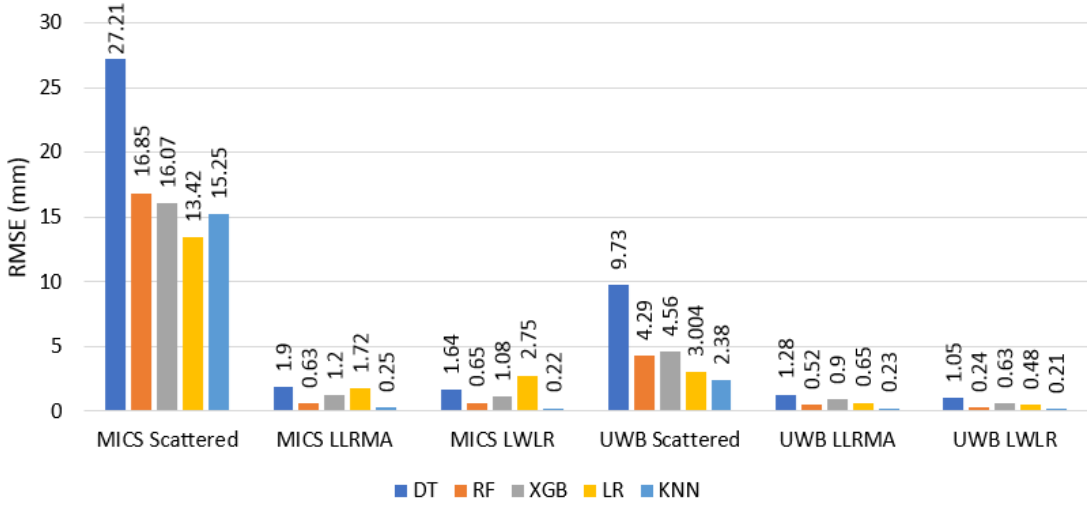

FIGURE 8. Improvement of accuracy using LLRMA and LWLR smoothing methods on both UWB and MICS path loss considering regular sensor topology (c).

improvement of accuracy, Figure 8 compares the RMSE using both scattered and smoothed path loss of UWB and MICS models with regular sensor topology (c). It is observed that the accuracy is improved significantly by applying the LLRMA and LWLR smoothing. The best accuracy is obtained using KNN on the LWLR smoothed path loss of UWB and MICS channel model with 0.21 *mm* and 0.22 *mm* RMSE, respectively.

C. PERFORMANCE USING IRREGULAR PATTERN

Considering the sensor receivers to be placed on the body surface, we apply the irregular pattern sensor topologies (e) and (f) as shown in Figure 2. That is, in irregular sensor topologies, sensor receivers are placed considering the original human body shape and curvatures. Table 8 presents the performance using topologies (e) and (f) in terms of RMSE and the computational times using both UWB and MICS path loss models. It is apparent from the results in Table 8 that using the irregular pattern sensor array, the localization accuracy improves significantly by applying the smoothing methods (LLRMA and LWLR) on both the UWB and MICS path loss as observed for the regular pattern as well. Among the ML regression methods, KNN performs the best with RMSE 0.21 *mm* and 0.22 *mm* using UWB and MICS channel models, respectively using LWLR smoothing.

D. PERFORMANCE WITH DIFFERENT DIMENSIONS

We also vary the dimension of the sensor array considering normal, overweight, and obese human body size as shown in Figure 3. The varying dimension of the sensor array and small intestine for the normal, overweight, and obese body size is summarized in Table 1. The evaluation scores using a normal body size are presented in Table 7. The evaluation scores for overweight and obese human bodies are included in Table 9. The RMSE using LWLR smoothed path loss with normal, overweight, and obese human body dimensions are compared in Figure 9. As we can see that the KNN performs the best for all dimensions of human body sizes using both MICS and UWB LWLR path loss models.

From the results as presented in Tables 6 to 9 for regular and irregular patterns of sensor topologies using different dimensions, it is observed that KNN performs the best among all the ML methods with low computational time. It is also observed from the results in Tables 6 to 9 that using 48 sensor receivers, the computational time taken by the ML methods using both scattered and smoothed path loss is almost the same. Thus, it is apparent that the computational time does not depend on the smoothing methods or dimensions, rather it depends on the dimensionality of the input data.

E. PERFORMANCE OF FEATURE SELECTION USING DIFFERENT NUMBER OF SENSOR RECEIVERS

We evaluate the performance of the WCE localization methods by varying the number of sensor receivers to vary the input features from 8 to 48 for each of the sensor topologies as shown in Figs. 2(c) and 2(f). The performance is also verified using 4 sensor receivers on the sensor array's front side (x-z plane). The number of sensor receivers is varied to select the most important and minimum required input features for WCE localization. The performances of the UWB and MICS path loss model with the regular pattern sensor topology (c) and irregular sensor topology (f) using the increasing number of sensor receivers are presented in Figures 10 and 11, respectively. As we can see in Figures 10 and 11 that for all the ML regression methods, the RMSE decreases with the increasing number of sensor receivers using both UWB and MICS scattered path loss. Whereas using smoothed path loss (LLRMA and LWLR), the performance slightly improves with the number of sensor receivers using all the ML regression methods of WCE localization. It is worth mentioning that using 4 sensor receivers, 0.22 *mm* and

TABLE 8. Evaluation scores using irregular pattern sensor topologies (e) and (f) with normal human body dimensions.

	Topology (e)						Topology (f)					
UWB models	Scattered		LLRMA		LWLR		Scattered		LLRMA		LWLR	
ML regression	RMSE (mm)	Time (s)	RMSE (mm)	Time (s)	RMSE (mm)	Time (s)	RMSE (mm)	Time (s)	RMSE (mm)	Time (s)	RMSE (mm)	Time (s)
DT	9.57	0.047	1.28	0.041	0.98	0.038	9.7	0.047	1.16	0.041	0.74	0.036
RF	4.22	3.54	0.32	3.09	0.23	2.82	4.18	3.25	0.35	2.99	0.27	2.71
XGB	4.39	3.82	0.87	4.41	0.57	4.20	4.4	1.94	0.87	1.86	0.57	1.91
LR	3.00	0.007	0.62	0.008	0.48	0.009	2.93	0.006	0.67	0.005	0.51	0.006
KNN	2.38	0.07	0.23	0.068	0.21	0.037	2.33	0.029	0.23	0.031	0.21	0.036
MICS models	Scattered		LLRMA		LWLR		Scattered		LLRMA		LWLR	
DT	22.33	0.051	1.47	0.04	1.82	0.04	22.77	0.051	2.05	0.042	1.23	0.042
RF	14.40	3.68	0.63	3.07	0.54	2.9	13.96	3.80	0.81	3.29	0.43	2.99
XGB	13.77	1.99	1.16	1.87	0.95	2.05	13.37	2.43	1.31	2.007	1.04	1.83
LR	11.99	0.007	1.15	0.006	2.002	0.006	11.56	0.007	1.17	0.008	1.99	0.007
KNN	12.92	0.026	0.25	0.032	0.22	0.036	12.40	0.033	0.25	0.032	0.22	0.034

TABLE 9. Evaluation scores using regular pattern sensor topology (c) with overweight and obese human body dimensions.

	Overweight						Obese					
UWB models	Scattered		LLRMA		LWLR		Scattered		LLRMA		LWLR	
	RMSE (mm)	Time (s)	RMSE (mm)	Time (s)	RMSE (mm)	Time (s)	RMSE (mm)	Time (s)	RMSE (mm)	Time (s)	RMSE (mm)	Time (s)
DT	11.35	0.045	2.03	0.04	1.21	0.037	13.97	0.047	2.06	0.043	1.56	0.037
RF	4.93	3.59	0.75	3.15	0.5	2.98	6.83	3.55	0.93	2.98	0.76	2.90
XGB	5.65	4.00	1.30	4.51	0.85	4.35	7.55	2.26	1.47	1.84	1.08	2.50
LR	3.83	0.006	0.87	0.007	0.67	0.009	4.85	0.007	0.95	0.007	0.70	0.009
KNN	2.39	0.08	0.34	0.069	0.32	0.038	3.82	0.057	0.34	0.032	0.33	0.035
MICS models	Scattered		LLRMA		LWLR		Scattered		LLRMA		LWLR	
DT	48.62	0.05	3.61	0.043	3.47	0.042	59.04	0.052	4.91	0.046	5.26	0.04
RF	30.98	3.98	1.37	3.28	1.76	3.27	38.71	4.10	2.17	3.45	2.23	3.40
XGB	29.86	4.09	2.13	4.69	1.93	4.61	39.10	4.11	2.90	4.73	2.54	4.65
LR	25.53	0.006	3.001	0.006	4.88	0.007	33.88	0.007	4.91	0.007	7.95	0.007
KNN	30.38	0.076	0.39	0.067	0.33	0.038	38.96	0.07	0.41	0.062	0.32	0.039

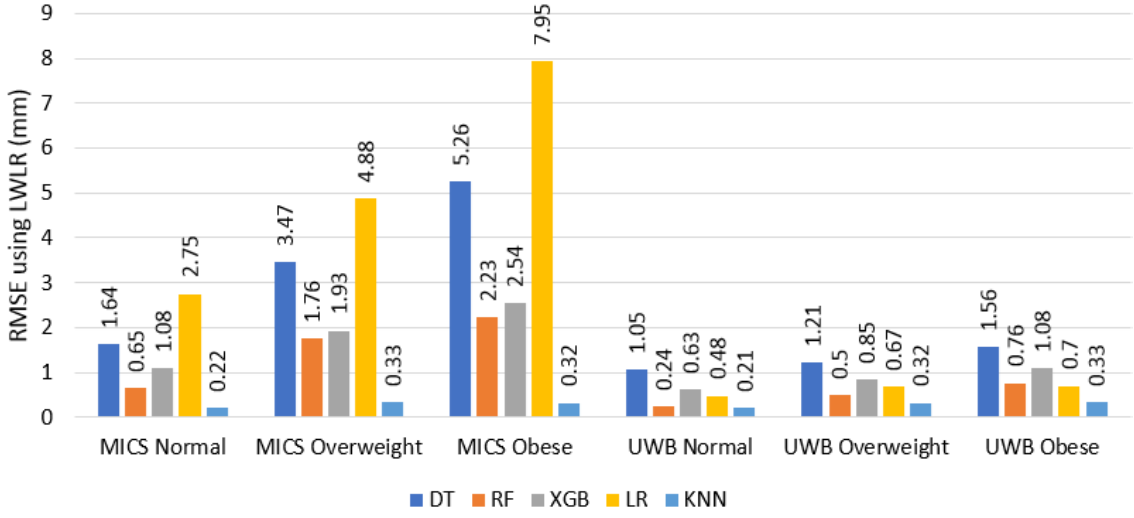

FIGURE 9. RMSE using the sensor array and small intestine dimension of normal, overweight, and obese human bodies.

1.32 *mm* RMSE are obtained using KNN on the LWLR smoothed path loss for UWB and MICS channel models, respectively. However, a drastic improvement in terms of RMSE is observed by using 8 sensor receivers compared to 4 sensor receivers for most of the cases. Thus it may be concluded for most of the cases that though the best accuracy is obtained using 48 input features or sensor receivers, a minimum of 8 sensor receivers (at the corner points of the

TABLE 10. Evaluation scores using regular sensor topology (c) and irregular sensor topology (f) with 8 sensor receivers.

	Topology (c) using 8 sensor receivers						Topology (f) using 8 sensor receivers					
UWB models	Scattered		LLRMA		LWLR		Scattered		LLRMA		LWLR	
ML regression	RMSE (mm)	Time (s)	RMSE (mm)	Time (s)	RMSE (mm)	Time (s)	RMSE (mm)	Time (s)	RMSE (mm)	Time (s)	RMSE (mm)	Time (s)
DT	10.219	0.014	1.303	0.014	1.081	0.009	10.2	0.012	0.93	0.01	0.868	0.01
RF	6.303	0.643	0.481	0.551	0.311	0.492	6.289	0.578	0.551	0.512	0.334	0.486
XGB	6.884	0.219	1.087	0.245	0.844	0.254	6.611	0.225	1.074	0.209	0.835	0.202
LR	6.349	0.004	1.387	0.005	1.209	0.003	6.469	0.003	1.732	0.003	1.489	0.003
KNN	5.71	0.007	0.355	0.005	0.219	0.005	5.684	0.007	0.348	0.004	0.22	0.004
MICS models	Scattered		LLRMA		LWLR		Scattered		LLRMA		LWLR	
DT	33.93	0.013	2.487	0.011	2.271	0.011	32.629	0.016	2.617	0.011	1.824	0.011
RF	24.20	0.593	1.358	0.526	0.915	0.537	23.07	0.675	1.326	0.551	0.933	0.557
XGB	25.58	0.216	2.02	0.209	1.661	0.232	24.73	0.249	1.895	0.23	1.49	0.249
LR	23.41	0.004	5.55	0.003	7.85	0.004	22.66	0.005	5.36	0.004	6.96	0.004
KNN	25.63	0.009	0.52	0.005	0.24	0.005	24.52	0.009	0.49	0.005	0.27	0.005

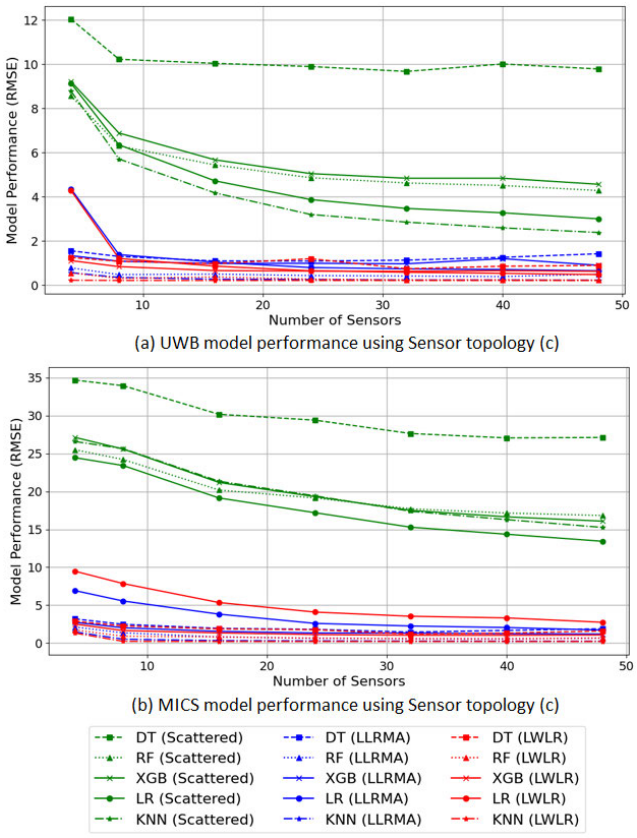

FIGURE 10. UWB and MICS model performance on sensor topology (c) using different number of sensor receivers.

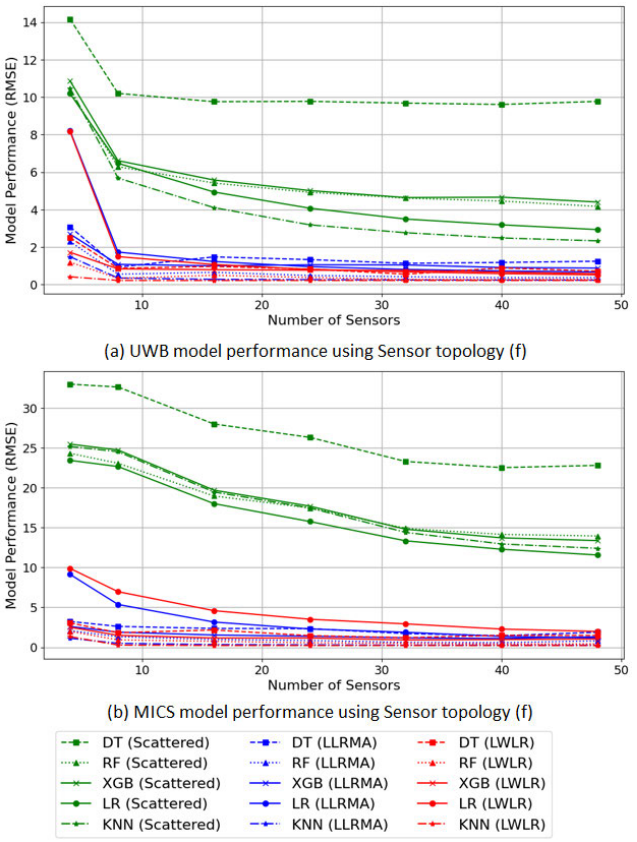

FIGURE 11. UWB and MICS model performance on sensor topology (f) using different number of sensor receivers.

sensor array) or input features are required to localize the WCE with reasonably high accuracy.

Table 10 includes the RMSE score and computational time using 8 sensor receivers of the corner points of the sensor topology (c) and (f) using both UWB and MICS path loss models. It is observed in Table 10 that using 8 sensor receivers, the computational time is reduced significantly as compared to the time taken using 48 sensor receivers as presented in Tables 7 and 8. It is also observed in Table 10 that using sensor topology (c), the linear regression (LR) method requires the least computational time of 0.003 sec and 0.004 sec to obtain 1.209 *mm* and 7.85 *mm* RMSE using UWB and MICS LWLR path loss, respectively using 8 sensor receivers. Whereas using 8 sensor receivers, KNN obtains the best accuracy with RMSE 0.219 *mm* in 0.005 sec and 0.23 mm in 0.005 sec using UWB and MICS LWLR path loss, respectively.

Table 11 compares the proposed WCE localization methods to the existing state-of-the-art works using different technologies. From the comparisons, it is observed in

TABLE 11. Comparison of the proposed method of WCE localization to other works in the literature.

Localization method	Datasets	No. of positions and dimension	Data processing or estimation	No. of sensor receivers or features	Classification or Regression	RMSE (mm)	Accuracy
Image or Video based methods							
Duda et al [41] 2007	Endoscopic images	7 2D	MPEG-7 homogeneous texture descriptor (HTD) feature extraction and principle component analysis (PCA) dimensionality reduction	62 HTD	Neural network	-	86.1%
Duda et al [42] 2007	Endoscopic images	4 2D	HTD feature extraction, Brute force (BF) and vector quantization (VQ)	BF-32 VQ-32	Neural network	-	95.19% (BF) 94.49% (VQ)
Dimas et al [43] 2017	97 video frames	196 mm 3D	Geometric visual odometry (VO) method	20 frames matched points	Multilayer feed-forward neural network (MFNN)	79±51	-
Chung et al [44] 2023	15,049 small bowel images	196 mm 3D		Transitional area features	Deep learning algorithm	-	87%
RF based methods							
Glukhovsky et al and Fischer et al [21], [22] 2002 & 2004	Measured RF signal strength	92 2D	RF triangulation	8	No	37.7	-
Ye et al [11] 2012	MICS band RSSI	1926 3D	RSSI based triangulation	64	No	34	-
Anzai et al [35] 2012	MICS band RSSI	9 3D	Maximum likelihood (ML) and Least square (LS) localization	14	No	70 (ML) and 100 (LS)	-
Pourhomayoun et al [34] 2013	MICS band spatial sparsity	500 2D	Convex optimization and l_1-norm minimization	16	No	8.8	-
Ito et al [36] 2014	MICS band RSSI	1000 3D	ML localization using FIR filter and particle filter	8	No	15 (FIR) and 7 (particle)	-
Hany et al [26] and [27] 2017	MICS band path loss	2530 3D	Path loss smoothing and path loss degree-based WCL	64	No	24.53 23.6	-
Bjørnevik et al [37] 2015	UWB band RSSI	10000 3D	Compressive sensing and VNL Kalman filter	24	No	35	-
Hany et al [28] 2017	UWB band path loss	2530 3D	GWA filter and MIMO for path loss estimation and position bounded calibrated WCL	56	No	8.24 (GWA) and 5.14 (MIMO)	-
Hany et al [29] 2018	UWB band path loss	2530 3D	ML based path loss estimation and WCL	56	No	6.2	-
Suveren et al [31] 2022	UWB band RSS	64 3D	RSS-based centroid algorithm	20	No	34.12	-
Hany et al [32] 2023	UWB band path loss	2443 3D	Smoothed path loss degree-based weighted centroid localization	48	yes	6.83	-
Proposed methods							
Proposed	MICS band path loss	2443 3D	LWLR data smoothing and k-fold cross validation	8* 48	DT RF XGB LR KNN	1.82* 0.93* 1.49* 6.96* 0.27* / 1.23 0.43 1.04 1.99 0.22	-
Proposed	UWB band path loss	2443 3D	LWLR data smoothing and k-fold cross validation	8* 48	DT RF XGB LR KNN	0.86* 0.33* 0.83* 1.48* 0.22* / 0.74 0.27 0.57 0.51 0.21	-

Table 11 that the proposed methods can localize the WCE with very high accuracy as compared to other RF-based methods in the literature. Among the proposed methods, KNN performs the best using both MICS and UWB LWLR smoothed path loss.

VIII. CONCLUSION

In this paper, we have proposed path loss-based WCE localization method using machine learning (ML) regression. First, we generated UWB and MICS band path loss data for 2443 3D positions of the WCE in the small intestine. Then, we applied local linear regression moving average (LLRMA) and local weighted linear regression (LWLR) for path loss data smoothing. Next, data labeling and concatenation have been applied for data manipulation. We varied the number of sensor receivers from 4 to 48 to select the required features and to analyze the computational time. The 5-fold cross-validation method has been applied to split the datasets into 5 sets and to evaluate the test accuracy using all the datasets. Finally, we have applied five ML regression methods namely DT, RF, XGB, LR, and KNN on the scattered as well as on the smoothed path loss data to detect the 3D position of the WCE. It is observed that the performance of the ML regression algorithms improved significantly by using both LLRMA and LWLR smoothing methods. Among the five ML algorithms, KNN performs the best with minimum RMSE in low computational time using both UWB and MICS band path loss features of 4 to 48 sensor receivers. We observed that the accuracy is improved slightly by increasing the number of sensor receivers or input features. However, a drastic improvement in terms of RMSE is observed by using 8 sensor receivers compared to 4 sensor receivers for most of the cases. From the evaluation results, it is found that using the irregular topology (f) with 8 sensor receivers, KNN performs with 0.22 *mm* and 0.27 *mm* RMSE in the least computational time 0.004 sec and 0.005 sec using LWLR smoothing on the UWB and MICS path loss models, respectively. Whereas by using 48 sensor receivers, KNN performs the best with 0.21 *mm* and 0.22 *mm* RMSE in 0.036 sec and 0.034 sec time using UWB and MICS channel models, respectively. Thus, it may be concluded that using our proposed method, significantly high localization accuracy is possible to be achieved in very low computational time using only 8 sensor receivers without any prior knowledge of the channel parameters or any unknown parameters and bounds, reference positions of sensor receivers, sensor placement topologies, and the dimensions. However, future works on practical validation of the proposed WCE localization method is required using real data and ground truth positions.

REFERENCES

[1] H. Mateen, R. Basar, A. U. Ahmed, and M. Y. Ahmad, "Localization of wireless capsule endoscope: A systematic review," *IEEE Sensors J.*, vol. 17, no. 5, pp. 1197–1206, Mar. 2017.

[2] Y. Guo and G. Shao, "Wireless localization for a capsule endoscopy: Techniques and solutions," in *Antenna and Sensor Technologies in Modern Medical Applications*. Wiley, 2021, pp. 191–234.

[3] G. Shao, Y. Tang, L. Tang, Q. Dai, and Y.-X. Guo, "A novel passive magnetic localization wearable system for wireless capsule endoscopy," *IEEE Sensors J.*, vol. 19, no. 9, pp. 3462–3472, May 2019.

[4] P. S. Boroujeni, H. N. Pishkenari, H. Moradi, and G. Vossoughi, "Model-aided real-time localization and parameter identification of a magnetic endoscopic capsule using extended Kalman filter," *IEEE Sensors J.*, vol. 21, no. 12, pp. 13667–13675, Jun. 2021.

[5] S. T. Goh, S. A. Zekavat, and K. Pahlavan, "DOA-based endoscopy capsule localization and orientation estimation via unscented Kalman filter," *IEEE Sensors J.*, vol. 14, no. 11, pp. 3819–3829, Nov. 2014.

[6] T. Ito, D. Anzai, and J. Wang, "Performance comparison between TOA- and RSSI-based localization methods for wireless capsule endoscopy systems," in *Proc. 9th Int. Symp. Med. Inf. Commun. Technol. (ISMICT)*, Mar. 2015, pp. 139–143.

[7] U. I. Khan, K. Pahlavan, and S. Makarov, "Comparison of TOA and RSS based techniques for RF localization inside human tissue," in *Proc. Annu. Int. Conf. IEEE Eng. Med. Biol. Soc.*, Aug. 2011, pp. 5602–5607.

[8] A. R. Nafchi, S. T. Goh, and S. A. R. Zekavat, "Circular arrays and inertial measurement unit for DOA/TOA/TDOA-based endoscopy capsule localization: Performance and complexity investigation," *IEEE Sensors J.*, vol. 14, no. 11, pp. 3791–3799, Nov. 2014.

[9] A. R. Nafchi, S. T. Goh, and S. A. R. Zekavat, "High performance DOA/TOA-based endoscopy capsule localization and tracking via 2D circular arrays and inertial measurement unit," in *Proc. IEEE Int. Conf. Wireless Space Extreme Environ.*, Nov. 2013, pp. 1–6.

[10] R. Chandra, A. J. Johansson, and F. Tufvesson, "Localization of an RF source inside the human body for wireless capsule endoscopy," in *Proc. 8th Int. Conf. Body Area Netw.*, 2013, pp. 48–54.

[11] Y. Ye, P. Swar, K. Pahlavan, and K. Ghaboosi, "Accuracy of RSS-based RF localization in multi-capsule endoscopy," *Int. J. Wireless Inf. Netw.*, vol. 19, no. 3, pp. 229–238, Sep. 2012.

[12] D. Anzai, S. Aoyama, and J. Wang, "Impact of propagation characteristics on RSSI-based localization for 400 MHz MICS band implant body area networks," in *Proc. 6th Int. Symp. Med. Inf. Commun. Technol. (ISMICT)*, Mar. 2012, pp. 1–4.

[13] G. Bao, K. Pahlavan, and L. Mi, "Hybrid localization of microrobotic endoscopic capsule inside small intestine by data fusion of vision and RF sensors," *IEEE Sensors J.*, vol. 15, no. 5, pp. 2669–2678, May 2015.

[14] A. Eshkevari and S. M. S. Sadough, "An improved method for localization of wireless capsule endoscope using direct position determination," *IEEE Access*, vol. 9, pp. 154563–154577, 2021.

[15] P. Oleksy and Ł. Januszkiewicz, "Wireless capsule endoscope localization with phase detection algorithm and adaptive body model," *Sensors*, vol. 22, no. 6, p. 2200, Mar. 2022.

[16] S. S. Vedaei and K. A. Wahid, "A localization method for wireless capsule endoscopy using side wall cameras and IMU sensor," *Sci. Rep.*, vol. 11, no. 1, pp. 1–16, May 2021.

[17] R. Chavez-Santiago, K. Sayrafian-Pour, A. Khaleghi, K. Takizawa, J. Wang, I. Balasingham, and H.-B. Li, "Propagation models for IEEE 802.15.6 standardization of implant communication in body area networks," *IEEE Commun. Mag.*, vol. 51, no. 8, pp. 80–87, Aug. 2013.

[18] A. Khaleghi, R. Chávez-Santiago, and I. Balasingham, "Ultra-wideband pulse-based data communications for medical implants," *IET Commun.*, vol. 4, no. 15, pp. 1889–1897, Oct. 2010.

[19] A. Khaleghi, R. Chávez-Santiago, and I. Balasingham, "Ultra-wideband statistical propagation channel model for implant sensors in the human chest," *IET Microw. Antennas Propag.*, vol. 5, no. 15, pp. 1805–1812, Dec. 2011.

[20] S. Perez-Simbor, C. Andreu, C. Garcia-Pardo, M. Frasson, and N. Cardona, "UWB path loss models for ingestible devices," *IEEE Trans. Antennas Propag.*, vol. 67, no. 8, pp. 5025–5034, Aug. 2019.

[21] A. Glukhovsky, M. Frisch, and D. Levy, "Array system and method for locating an in vivo signal source," U.S. Patent 7 618 366, Jan. 2002.

[22] D. Fischer, R. Schreiber, D. Levi, and R. Eliakim, "Capsule endoscopy: The localization system," *Gastrointestinal Endoscopy Clinics North Amer.*, vol. 14, no. 1, pp. 25–31, Jan. 2004.

[23] U. Hany and K. A. Wahid, "An adaptive linearized method for localizing video endoscopic capsule using weighted centroid algorithm," *Int. J. Distrib. Sensor Netw.*, vol. 11, no. 3, Mar. 2015, Art. no. 342428.

[24] U. Hany, L. Akter, and F. Hossain, "Degree-based WCL for video endoscopic capsule localization," *IEEE Sensors J.*, vol. 17, no. 9, pp. 2904–2916, May 2017.

[25] U. Hany and L. Akter, "Local parametric approach of wireless capsule endoscope localization using randomly scattered path loss based WCL," *Wireless Commun. Mobile Comput.*, vol. 2017, pp. 1–17, 2017.
[26] U. Hany and L. Akter, "Non-parametric method of path loss estimation for endoscopic capsule localization," *Int. J. Wireless Inf. Netw.*, vol. 25, no. 1, pp. 44–56, Mar. 2018.
[27] U. Hany and L. Akter, "Accuracy of endoscopic capsule localization using position bounds on smoothed path loss based WCL," in *Proc. IEEE Int. Conf. Signal Image Process. Appl. (ICSIPA)*, Sep. 2017, pp. 553–558.
[28] U. Hany and L. Akter, "Non-parametric approach of video capsule endoscope localization using suboptimal method of position bounded CWCL," *IEEE Sensors J.*, vol. 17, no. 20, pp. 6806–6815, Oct. 2017.
[29] U. Hany and L. Akter, "Non-parametric approach using ML estimated path loss bounded WCL for video capsule endoscope localization," *IEEE Sensors J.*, vol. 18, no. 11, pp. 4761–4769, Jun. 2018.
[30] P. Brida and J. Machaj, "A novel enhanced positioning trilateration algorithm implemented for medical implant in-body localization," *Int. J. Antennas Propag.*, vol. 2013, pp. 1–10, Jan. 2013.
[31] M. Suveren, R. Akay, and M. Kanaan, "Localization of an ultra wide band wireless endoscopy capsule inside the human body using received signal strength and centroid algorithm," *Int. J. Optim. Control, Theories Appl.*, vol. 12, no. 2, pp. 151–159, Jul. 2022.
[32] U. Hany and L. Akter, "Accuracy of UWB path loss-based localization of wireless capsule endoscopy," *J. Healthcare Eng.*, vol. 2023, pp. 1–13, Jun. 2023.
[33] J. Shi and J. Wang, "Channel characterization and diversity feasibility for in-body to on-body communication using low-band UWB signals," in *Proc. 3rd Int. Symp. Appl. Sci. Biomed. Commun. Technol.*, Nov. 2010, pp. 1–4.
[34] M. Pourhomayoun, Z. Jin, and M. L. Fowler, "Accurate localization of in-body medical implants based on spatial sparsity," *IEEE Trans. Biomed. Eng.*, vol. 61, no. 2, pp. 590–597, Feb. 2014.
[35] D. Anzai, S. Aoyama, and J. Wang, "Performance evaluation on RSSI-based localization for capsule endoscopy systems with 400 MHz MICS band signals," *IEICE Trans. Commun.*, vol. 95, no. 10, pp. 3081–3087, 2012.
[36] T. Ito, D. Anzai, and J. Wang, "Performance evaluation on RSSI-based wireless capsule endoscope location tracking with particle filter," *IEICE Trans. Commun.*, vol. 97, no. 3, pp. 579–586, 2014.
[37] A. S. Bjørnevik, "Localization and tracking of intestinal paths for wireless capsule endoscopy," M.S. thesis, Norwegian Univ. Sci. Technol., Trondheim, Norway, 2015, pp. 75–83.
[38] N. Inayat, M. Khan, N. Iqbal, S. Khan, M. Raza, D. M. Khan, A. Khan, and D. Q. Wei, "IEnhancer-DHF: Identification of enhancers and their strengths using optimize deep neural network with multiple features extraction methods," *IEEE Access*, vol. 9, pp. 40783–40796, 2021.
[39] S. Khan, M. Khan, N. Iqbal, M. Li, and D. M. Khan, "Spark-based parallel deep neural network model for classification of large scale RNAs into piRNAs and non-piRNAs," *IEEE Access*, vol. 8, pp. 136978–136991, 2020.
[40] F. Khan, M. Khan, N. Iqbal, S. Khan, D. Muhammad Khan, A. Khan, and D.-Q. Wei, "Prediction of recombination spots using novel hybrid feature extraction method via deep learning approach," *Frontiers Genet.*, vol. 11, Sep. 2020, Art. no. 539227.
[41] K. Duda, T. Zielinski, R. Fraczek, J. Bulat, and M. Duplaga, "Localization of endoscopic capsule in the GI tract based on MPEG-7 visual descriptors," in *Proc. IEEE Int. Workshop Imag. Syst. Techn.*, Mar. 2007, pp. 1–4.
[42] K. Duda, T. Zielinski, M. Duplaga, M. Grega, and M. Leszczuk, "VQ classification based on MPEG-7 visual descriptors for video endoscopic capsule localization in the gastrointestinal tract," in *Proc. 15th Eur. Signal Process. Conf.*, Sep. 2007, pp. 1397–1401.
[43] G. Dimas, D. K. Iakovidis, G. Ciuti, A. Karargyris, and A. Koulaouzidis, "Visual localization of wireless capsule endoscopes aided by artificial neural networks," in *Proc. IEEE 30th Int. Symp. Comput.-Based Med. Syst. (CBMS)*, Jun. 2017, pp. 734–738.
[44] J. Chung, D. J. Oh, J. Park, S. H. Kim, and Y. J. Lim, "Automatic classification of GI organs in wireless capsule endoscopy using a no-code platform-based deep learning model," *Diagnostics*, vol. 13, no. 8, p. 1389, Apr. 2023.
[45] K. Sayrafian-Pour, W.-B. Yang, J. Hagedorn, J. Terrill, and K. Y. Yazdandoost, "A statistical path loss model for medical implant communication channels," in *Proc. IEEE 20th Int. Symp. Pers., Indoor Mobile Radio Commun.*, Sep. 2009, pp. 2995–2999.
[46] *Local Regression Smoothing*. Accessed: Jun. 7, 2023. [Online]. Available: https://www.mathworks.com/help/curvefit/smoothing-data.html
[47] Wikipedia. *Weighted Least Squares*. Accessed: Jun. 7, 2023. [Online]. Available: https://en.wikipedia.org/wiki/Weighted_least_squares
[48] J. Brownlee. *A Gentle Introduction to K-Fold Cross-Validation*. Accessed: Jun. 9, 2023. [Online]. Available: https://machinelearningmastery.com/k-fold-cross-validation/
[49] V. Kurama. *Regression in Machine Learning: What it is and Examples of Different Models*. Accessed: Jun. 7, 2023. [Online]. Available: https://builtin.com/data-science/regression-machine-learning
[50] A. Ohri. *10 Popular Regression Algorithms in Machine Learning of 2022*. Accessed: Jun. 9, 2023. [Online]. Available: https://u-next.com/blogs/machine-learning/popular-regression-algorithms-ml/
[51] *10 Machine Learning Algorithms to Know in 2023*. Accessed: Jun. 9, 2023. [Online]. Available: https://www.coursera.org/articles/machine-learning-algorithms

UMMA HANY received the Ph.D. degree in electrical and electronic engineering (EEE) from the Bangladesh University of Engineering and Technology (BUET), in 2017.

After her graduation, she was with IICT, BUET, and Huawei Technologies Bangladesh Ltd. She was also with the Department of EEE, University of Asia–Pacific, and the Bangladesh Army International University of Science and Technology, as a Lecturer, an Assistant Professor, and an Associate Professor. She also pursued research as a Visiting Scholar with the University of Saskatchewan under the Canadian Commonwealth Scholarship Program. Currently, she is an Associate Professor with the Department of EEE, Ahsanullah University of Science and Technology. She has several publications in peer-reviewed journals and conferences. Her research interests include artificial intelligence, wireless sensor networks, wireless communication, localization, pattern recognition, biomedical signal, and image processing.

NAFE MUHTASIM HYE received the B.Sc. degree in electrical and electronic engineering (EEE) from the Ahsanullah University of Science and Technology (AUST). Currently, he is pursuing research as a Graduate Research Assistant with the Department of EEE, AUST. His research interests include artificial intelligence, machine learning, deep learning, and biomedical signal and image processing. He was one of the founding members of the university's Mars Rover team, which finished 26th out of more than 65 competitors globally and fourth in Asia in the European Rover Challenge, Poland, supported by NASA and the Mars Society. He also completed an internship in corporate banking and banking information technology from one of the most reputed banks in Bangladesh.

LUTFA AKTER received the Ph.D. degree in electrical engineering from Kansas State University, USA, in 2010. She is currently a Professor with the Department of Electrical and Electronic Engineering (EEE), Bangladesh University of Engineering and Technology (BUET). Her current research interests include biomedical signal processing, cell free massive MIMO, wireless sensor deployment, the IoT, and localization of wireless video capsule endoscope.